


Stability of traveling waves of a thermoviscous liquid film down the outer surface of a cylinder

Garima Singh and Naveen Tiwari 

Department of Chemical Engineering, Indian Institute of Technology, Kanpur, Kanpur 208016, India



(Received 19 October 2023; accepted 10 January 2024; published 13 February 2024)

A liquid film coating a cylindrical substrate is unstable to interfacial disturbances governed by Rayleigh-plateau instability. These initial disturbances grow in time and, beyond saturation, develop into a train of droplets of equal amplitude that move downstream at the same velocity. The traveling wave profiles, formed by a thermoviscous fluid as it flows down the exterior of a nonisothermal vertical cylinder, are computed as a function of various parameters. Further, this study investigates the stability behavior of these traveling waves. An unstable film leads to the formation of an axially asymmetric pattern. The influence of the thermoviscous nature of the fluid, along with the Biot number, Marangoni number, and Bond number, has been investigated. Linear stability analysis is performed by perturbing the axisymmetric traveling wave solution in the azimuthal direction. It is shown that while a gravity mode exists at small wave numbers, a thermocapillary mode exists at large wave numbers. The streamline patterns are shown to be consistent with the presence of the thermocapillary mode. The nonlinear analysis shows that the chosen pattern of instability does not correspond to the largest growth rate but is governed by the wavelength conforming to the periodic confinement in the azimuthal direction. An interesting pattern evolves in the presence of more than one such conforming wavelength.

DOI: [10.1103/PhysRevFluids.9.024002](https://doi.org/10.1103/PhysRevFluids.9.024002)

I. INTRODUCTION

A gravity driven viscous liquid film over a fiber or cylinder is unstable to infinitesimal interfacial disturbances. The surface tension driven instability is the Rayleigh-Plateau instability (RPI) that leads to the formation of liquid beads on the cylinder. The problems show rich nonlinear dynamics and lead to interesting features such as traveling wave solutions [1,2], symmetric [3,4] and asymmetric [5] bead formation, etc. Thin viscous films flowing outside of a cylinder are utilized in a variety of applications, such as coating or patterning of a wire [6], cooling optical fibers [7], and as a fluid layer present on the surface of heat transfer devices [8]. Thus the fluid pattern formed on the surface of the substrate can have a considerable impact on its effectiveness, and hence it is desirable to understand the stability behavior of the film and subsequent pattern evolution.

Flow of a noninertial thin film over a cylindrical substrate has been investigated recently by several researchers [9–13]. Quéré [3] was the first to study and propose a saturation limit at which the drop formation due to the Rayleigh-Plateau instability was suppressed for asymptotically thin films. Subsequent studies have analyzed the stability of the film flow over a cylinder [1,4,11,12,14]. In the work of Kliakhandler *et al.* [4], a theoretical and experimental investigation was carried out. The film was considered noninertial; however, the full curvature term was included in the normal stress balance, which allowed them to compare the results for a thin film with those for a thick film. Craster and Matar [1] obtained a similar evolution equation using an approximated curvature similar to the formulation for viscous threads and jets. A traveling wave solution was found using an eigenvalue problem for wave velocity. Using this approach, they were able to predict several solution regimes for this problem. A spatiotemporal stability analysis for this system was first conducted by

Duprat *et al.* [11]. They used the evolution equation for sufficiently thin films from the work of Frenkel [14] to obtain a dispersion relation. Subsequently, they applied Briggs criteria and reported the critical condition of the instability transition from absolute to convective instability. A similar transition condition was found for a thick film using the approach of Kliakhandler *et al.* [4]. In their study, regular wave train patterns were formed for the absolutely unstable system, while an irregular wave train was observed for the convective instability.

Most of the applications mentioned above require nonisothermal conditions. The substrate is usually at a higher or lower temperature than the film coating it. Any nonuniformity in the film thickness along the substrate leads to nonuniformity in the temperature and thus to the generation of thermocapillary stress at the liquid-gas interface [15,16]. Ding *et al.* [17] extended the thin film model of Duprat *et al.* [11] and accounted for the effect of the thermocapillary stress on the spatiotemporal stability. They modeled the nonlinear film dynamics and concluded the supportive role of absolute instability in film rupture. For a thermoviscous liquid, there have been studies to account for the effect of temperature on viscosity by assuming an exponential dependence of temperature on the viscosity [18–20]. Khanum and Tiwari [21] implemented this temperature-dependent viscosity in the thin-film model and demonstrated that the spatiotemporal stability of the film is strongly influenced by the thermocapillary nature of the liquid. Kishal and Tiwari [22] followed the method of Kliakhandler *et al.* [4] and accounted for full curvature in the normal stress balance and extended the work of Khanum and Tiwari [21] for thicker films. They concluded that the instability evolves into traveling waves beyond nonlinear saturation.

This work explores the traveling wave profiles over a vertical cylinder and their stability behavior. The axisymmetric profiles are computed using a shooting method, and the effect of various parameters is studied on the film profile and the wave speed. An unstable traveling wave leads to an asymmetric pattern on the vertical cylinder. The stability is analyzed over a range of parameters, and the nonlinear evolution of the pattern is investigated. The paper is organized as follows. Problem formulation and the analytical model derived within the lubrication approximation are detailed in Sec. II, followed by the steady-state solution of the evolution equation in Sec. III. Linear stability analysis has been detailed in Sec. IV. Lastly, the nonlinear computations are illustrated in Sec. V, followed by the discussion in Sec. VI and conclusions in Sec. VII.

II. PROBLEM FORMULATION

A thin film of thermoviscous fluid is considered flowing down the outside surface of a vertical cylinder of radius R under the effect of gravity as shown in Fig. 1. The cylinder surface is at a temperature $T = T_s$, and the ambient air temperature is $T = T_\infty$. The fluid is assumed incompressible with density ρ , and the dynamic viscosity has been considered to be an exponential function of temperature [19,23]:

$$\mu = \mu_0 \exp \left[\frac{-\lambda(T - T_s)}{\mu_0} \right]. \quad (1)$$

In this relation, μ_0 is the viscosity of the fluid at the surface temperature ($T = T_s$) of the solid cylinder, and λ is a positive constant that represents the change in dynamic viscosity with a change in temperature, i.e., $\lambda = -d\mu/dT$ at $T = T_s$. The surface tension Υ has been considered to be linearly dependent on temperature,

$$\Upsilon(T) = \Upsilon_0 + \Upsilon_T(T - T_\infty), \quad (2)$$

where Υ_0 is the surface tension at the ambient temperature T_∞ and the constant $\Upsilon_T = d\Upsilon/dT (< 0)$.

The bulk fluid flows axially downward along the z axis. The radial coordinate is given by r , while θ represents the azimuthal direction. The thickness of the film, in general, varies with time (t), axial (z), and azimuthal (θ) coordinates. The film thickness is assumed to be much smaller than the cylinder radius.

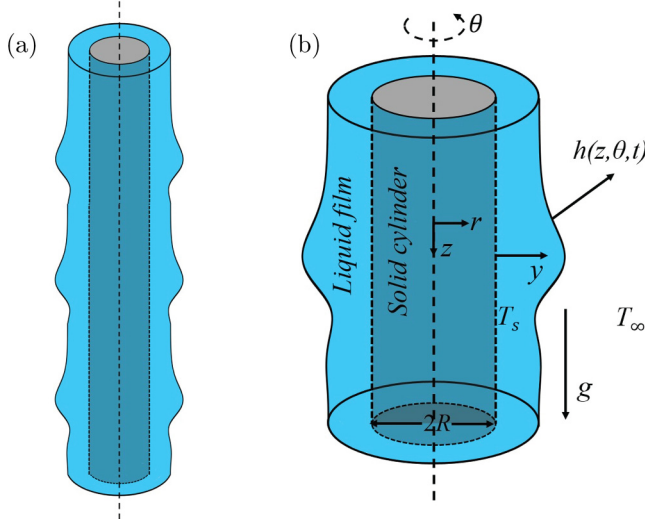


FIG. 1. Schematic of the flow geometry: (a) a series of traveling waves and (b) a qualitative pattern of one traveling wave on the outside surface of a vertical solid cylinder.

The equations governing the flow are the continuity equation, Navier-Stokes equation, and energy equation given in Eqs. (3), (4), and (5), respectively:

$$\nabla \cdot \mathbf{u} = 0, \quad (3)$$

$$\rho \frac{\partial \mathbf{u}}{\partial t} + \rho \mathbf{u} \cdot \nabla \mathbf{u} = -\nabla p + \nabla \cdot (\mu \nabla \mathbf{u}) + \rho \mathbf{g}, \quad (4)$$

$$\frac{\partial T}{\partial t} + \mathbf{u} \cdot \nabla T = (k_{th}/\rho C_p) \nabla^2 T. \quad (5)$$

In the equations above, $\mathbf{u} = (u_r, u_\theta, u_z)$ is the velocity vector, where u_r is the radial, u_θ is the azimuthal, and u_z represents the axial components of the velocity vector, and p is the pressure. The temperature across the film, $T(r, \theta, z, t)$, has been assumed to vary with space and time. C_p and k_{th} in the energy equation are specific heat capacity and thermal conductivity of the fluid, which are assumed to be constant.

The usual no-slip and no-penetration boundary conditions at the liquid-solid interface ($r = R$) are used to solve for the velocity field,

$$\mathbf{u} = 0, \quad (6)$$

and the liquid-gas interface [$r = R + h(\theta, z, t)$] is subjected to stress balance in the normal direction and in two tangential directions as shown below in Eqs. (7), (8), and (9), respectively:

$$-p + \mathbf{n} \cdot \boldsymbol{\tau} \cdot \mathbf{n} = -\gamma \nabla_s \cdot \mathbf{n}, \quad (7)$$

$$\mathbf{t}_\theta \cdot \boldsymbol{\tau} \cdot \mathbf{n} = \mathbf{t}_\theta \cdot \nabla_s \gamma, \quad (8)$$

$$\mathbf{t}_z \cdot \boldsymbol{\tau} \cdot \mathbf{n} = \mathbf{t}_z \cdot \nabla_s \gamma. \quad (9)$$

Here, $\boldsymbol{\tau}$ is the viscous stress tensor and can be defined as $\boldsymbol{\tau} = \mu(\nabla \mathbf{u} + \nabla \mathbf{u}^T)$. \mathbf{n} is the unit vector normal to the liquid air interface, pointing in an outward direction at the free surface of the liquid. \mathbf{t}_θ and \mathbf{t}_z are the tangential stress vectors in azimuthal and axial directions, respectively, at the free surface. The surface gradient operator used in the stress balances can be defined as $\nabla_s = (\mathbf{I} - \mathbf{nn}) \cdot \nabla$, where \mathbf{I} is the identity matrix.

The energy balance equation, Eq. (5), is associated with temperature conditions at the solid-liquid interface and convective boundary conditions at the liquid-air interface:

(1) At the solid-liquid interface ($r = R$)

$$T = T_s, \quad (10)$$

(2) At the liquid-air interface [$r = R + h(\theta, z, t)$]

$$-k_{th} \nabla T^i \cdot \mathbf{n} = h_f (T^i - T_\infty), \quad (11)$$

where h_f represents the heat transfer coefficient at the liquid-gas interface and k_{th} is the film's thermal conductivity. T^i is the temperature at the liquid-air interface, i.e., $T^i = T(r = R + h)$.

The evolution equation for the free surface of the film can be obtained by making use of kinematic boundary conditions at the liquid-air interface,

$$\frac{\partial h}{\partial t} + \frac{u_\theta}{r} \frac{\partial h}{\partial \theta} + u_z \frac{\partial h}{\partial z} = u_r. \quad (12)$$

The average film thickness far from the capillary ridge is denoted by H_0 . A new dimensionless radial coordinate, $y = r - R$ (as shown in Fig. 1), is introduced such that $y = 0$ is at the outside surface of the cylinder and $y = h$ is the liquid-gas interface. The radius of the cylinder, R , is considered as the characteristic length, and $U_z = (\rho g H_0^2 / \mu_0)$ is taken as the velocity scale. Here H_0 is taken as the length scale along the y -direction. The nondimensional variables in this work are as follows:

$$\hat{y} = \frac{(\hat{r} - 1)}{\epsilon}, \quad \hat{r} = \frac{r}{R}, \quad \hat{z} = \frac{z}{R}, \quad \epsilon = \frac{H_0}{R}, \quad \hat{T} = \frac{(T - T_\infty)}{(T_s - T_\infty)}, \quad (13)$$

$$\hat{h} = \frac{h}{H_0}, \quad \hat{u}_z = \frac{u_z}{U_z}, \quad \hat{u}_\theta = \frac{u_\theta}{U_z}, \quad \hat{u}_r = \frac{u_r}{\epsilon U_z}, \quad (14)$$

where \hat{r} and \hat{z} are the dimensionless radial and axial coordinates. The pressure scale used here is $\rho g R$ and the time scale is $R \mu_0 / \rho g H_0^2$. Lubrication or thin-film approximation ($\epsilon \ll 1$ and $\epsilon \text{Re} \ll 1$) has been employed in order to simplify the equations. Here the Reynolds' number $\text{Re} = \rho U_z H_0 / \mu_0$. Within the lubrication assumption, the continuity equation reduces to Eq. (15) and the Navier-Stokes equation reduces to Eqs. (16), (17), and (18):

$$\frac{\partial u_r}{\partial y} + \frac{\partial u_\theta}{\partial \theta} + \frac{\partial u_z}{\partial z} = 0, \quad (15)$$

$$\frac{\partial p}{\partial y} = 0, \quad (16)$$

$$\frac{\partial p}{\partial \theta} = \frac{\partial(\mu \partial u_\theta / \partial y)}{\partial y}, \quad (17)$$

$$\frac{\partial p}{\partial z} = 1 + \frac{\partial(\mu \partial u_z / \partial y)}{\partial y}. \quad (18)$$

The decoration sign $\hat{\cdot}$ has been eliminated from the dimensionless variables for clarity. No-slip and no-penetration boundary conditions are modified into their dimensionless form,

$$u_r = 0, \quad (19)$$

$$u_\theta = 0, \quad (20)$$

$$u_z = 0. \quad (21)$$

Within the lubrication approximation, the normal stress balance given in Eq. (7) simplifies into Eq. (22), and the two tangential stress balances will reduce into Eqs. (23) and (24). The kinematic

boundary condition in its dimensionless form within the lubrication approximation is given in Eq. (25):

$$p = -\text{Bo}^{-1} \left(-\epsilon^{-1} + h + \frac{\partial^2 h}{\partial \theta^2} + \frac{\partial^2 h}{\partial z^2} \right), \quad (22)$$

$$\mu \frac{\partial u_\theta}{\partial y} = -\epsilon \frac{\Delta T \Upsilon_T}{\mu_0 U_z} \frac{\partial T_i}{\partial \theta}, \quad (23)$$

$$\mu \frac{\partial u_z}{\partial y} = -\epsilon \frac{\Delta T \Upsilon_T}{\mu_0 U_z} \frac{\partial T_i}{\partial z}, \quad (24)$$

$$u_r = \frac{\partial h}{\partial t} + u_\theta \frac{\partial h}{\partial \theta} + u_z \frac{\partial h}{\partial z}. \quad (25)$$

In the above equations, Bond number, $\text{Bo} = \rho g R^2 / (\Upsilon_0 \epsilon)$, quantifies the relative strength of gravity to surface tension. Within the assumption that $\epsilon \text{Pe} \ll 1$, the energy equation is simplified to

$$\frac{\partial^2 T}{\partial y^2} = 0, \quad (26)$$

where $\text{Pe} = \rho C_p U_z H_0 / k_{th}$ is the Péclet number. The boundary conditions associated with the energy equation are modified to their dimensionless forms, at the cylinder surface $y = 0$,

$$T = 1, \quad (27)$$

and at the liquid-air interface $y = h$,

$$\frac{\partial T}{\partial y} = -\text{Bi}T, \quad (28)$$

where $\text{Bi} = h_f H_0 / k_{th}$ is the Biot number, which signifies the ratio of conductive resistance inside the film to the convective resistance at the liquid-gas interface. Temperature distribution inside the liquid film is obtained by integrating Eq. (26) with the boundary conditions given in Eq. (27) at $y = 0$ and Eq. (28) at $y = h$:

$$T = \frac{1 + \text{Bi}(h - y)}{1 + \text{Bi}h}. \quad (29)$$

Thus the temperature varies linearly along y -direction inside the film. This temperature profile is utilized to model the viscosity variation inside the film using Eq. (1) as

$$\mu = \exp[-V(T - 1)] = \exp(\eta y), \quad (30)$$

where μ is dimensionless viscosity which is obtained by scaling the dynamic viscosity by μ_0 . The thermoviscosity number is $V = \lambda \Delta T / \mu_0$, quantifying viscosity's dependence on temperature. It must be noted that $V < 0$ for a cooled substrate, while $V > 0$ for a heated substrate. Thermoviscous effects appear in the model through η where

$$\eta = \frac{V \text{Bi}}{1 + \text{Bi}h}. \quad (31)$$

The temperature at the liquid-gas interface is obtained using Eq. (29), and substituting $y = h$,

$$T(y = h) = T^i = \frac{1}{1 + \text{Bi}h}. \quad (32)$$

Axial and azimuthal components of velocity have been obtained by integrating their respective components of the Navier-Stokes equation, i.e., Eqs. (17) and (18), with the simplified stress balance boundary conditions given in Eqs. (22)–(24):

$$u_\theta = -\left(\text{Bo}^{-1} \frac{\partial h}{\partial \theta} + \text{Bo}^{-1} \frac{\partial^3 h}{\partial \theta \partial z^2} + \text{Bo}^{-1} \frac{\partial^3 h}{\partial \theta^3}\right) \left[\frac{(h-y) \exp(-\eta y)}{\eta} - \frac{\exp(-\eta y)}{\eta^2} - \frac{h}{\eta} + \frac{1}{\eta^2} \right] + \text{Ma} \frac{\partial T^i}{\partial \theta} \left(\frac{\exp(-\eta y)}{\eta} - \frac{1}{\eta} \right), \quad (33)$$

$$u_z = -\left(1 + \text{Bo}^{-1} \frac{\partial h}{\partial z} + \text{Bo}^{-1} \frac{\partial^3 h}{\partial z \partial \theta^2} + \text{Bo}^{-1} \frac{\partial^3 h}{\partial z^3}\right) \left[\frac{(h-y) \exp(-\eta y)}{\eta} - \frac{\exp(-\eta y)}{\eta^2} - \frac{h}{\eta} + \frac{1}{\eta^2} \right] + \text{Ma} \frac{\partial T^i}{\partial z} \left(\frac{\exp(-\eta y)}{\eta} - \frac{1}{\eta} \right), \quad (34)$$

where $\text{Ma} = -\epsilon \Delta T \Upsilon_T / (\mu_0 U_z)$ is the Marangoni number, which quantifies the contribution of the thermocapillary effect. Now using the above velocity components, fluid flux can be calculated in both directions. The azimuthal flux, $Q_\theta(z, \theta, t) = \int_0^h u_\theta dy$, is

$$Q_\theta(z, \theta, t) = -\left(\text{Bo}^{-1} \frac{\partial h}{\partial \theta} + \text{Bo}^{-1} \frac{\partial^3 h}{\partial \theta \partial z^2} + \text{Bo}^{-1} \frac{\partial^3 h}{\partial \theta^3}\right) \left(\frac{2h}{\eta^2} - \frac{h^2}{\eta} - \frac{2}{\eta^3} + \frac{2}{\eta^3} \exp(-\eta h) \right) - \text{Ma} \frac{\partial T^i}{\partial \theta} \left(\frac{h}{\eta} - \frac{1}{\eta^2} + \frac{\exp(-\eta h)}{\eta^2} \right), \quad (35)$$

and the axial flux, $Q_z(z, \theta, t) = \int_0^h u_z dy$, is

$$Q_z(z, \theta, t) = -\left(1 + \text{Bo}^{-1} \frac{\partial h}{\partial z} + \text{Bo}^{-1} \frac{\partial^3 h}{\partial z \partial \theta^2} + \text{Bo}^{-1} \frac{\partial^3 h}{\partial z^3}\right) \left(\frac{2h}{\eta^2} - \frac{h^2}{\eta} - \frac{2}{\eta^3} + \frac{2}{\eta^3} \exp(-\eta h) \right) - \text{Ma} \frac{\partial T^i}{\partial z} \left(\frac{h}{\eta} - \frac{1}{\eta^2} + \frac{\exp(-\eta h)}{\eta^2} \right). \quad (36)$$

Using the continuity equation, Eq. (15), the kinematic boundary condition, Eq. (25), can be written as a thin-film evolution equation as

$$\frac{\partial h}{\partial t} + \frac{\partial Q_\theta}{\partial \theta} + \frac{\partial Q_z}{\partial z} = 0. \quad (37)$$

III. STEADY-STATE SOLUTION

A. Film evolution equation

In order to find the two-dimensional solution, the film is assumed to be uniform in the azimuthal direction, and the solution is obtained by substituting $h(\theta, z, t) = h_0(z, t)$ in the evolution equation Eq. (37):

$$\frac{\partial h}{\partial t} = -\frac{\partial}{\partial z} \int_0^h u_z dy = -\frac{\partial Q_z}{\partial z}. \quad (38)$$

The traveling wave moves with a uniform velocity along the axial direction. The wave speed is denoted by c_w , and the steady-state solution is obtained in a copropagating traveling wave frame of speed c_w by introducing a new coordinate $\xi = z - c_w t$. Integration of Eq. (38) in the copropagating traveling wave frame with the condition that $h \rightarrow 1$ far from the disturbance ($\xi \rightarrow \infty$) results in

$$\frac{d^3 h_0}{d\xi^3} = -\left(\text{Bo} + \frac{dh_0}{d\xi}\right) + \frac{\text{Bo}(h_0 - 1)c_w}{g(h_0)} + \frac{\text{Bo}f(\eta)}{g(h_0)} + \frac{\text{MaBiBo}}{(1 + \text{Bi}h_0)^2} \frac{dh_0}{d\xi} \frac{H(h_0)}{g(h_0)}, \quad (39)$$

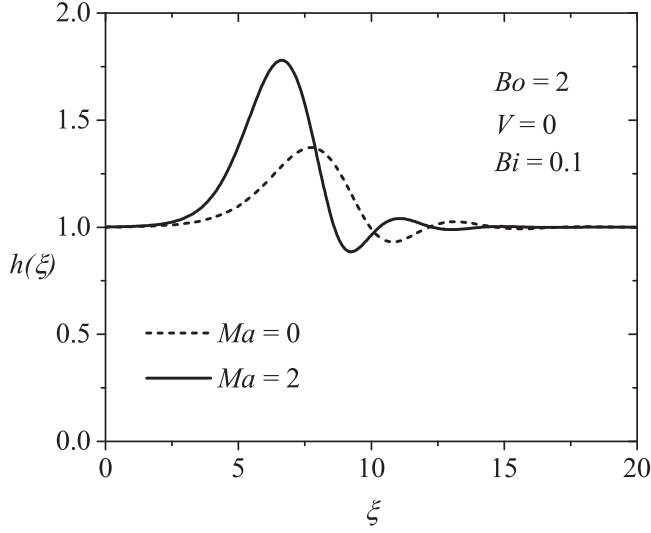


FIG. 2. Traveling wave profile obtained in the absence of thermoviscous effects for $V = 0$, $Bi = 0.1$, and $Bo = 2$. The wave speeds are $c_w = 1.3$ for $Ma = 0$ and $c_w = 1.67$ for $Ma = 2$.

where $f(\eta) = Q_z(h = 1)$:

$$\begin{aligned} f(\eta) &= -\left[\frac{2}{\eta^2} - \frac{1}{\eta} - \frac{2}{\eta^3} + \frac{2}{\eta^3} \exp(-\eta) \right], \\ g(h_0) &= -\left[\frac{2h_0}{\eta^2} - \frac{h_0^2}{\eta} - \frac{2}{\eta^3} + \frac{2}{\eta^3} \exp(-\eta h_0) \right], \\ H(h_0) &= -\left[\frac{h_0}{\eta} - \frac{1}{\eta^2} + \frac{\exp(-\eta h_0)}{\eta^2} \right]. \end{aligned}$$

For weak thermoviscous effects ($V \rightarrow 0$), the above equation can be simplified to

$$\frac{d^3 h_0}{d\xi^3} = -\left(Bo + \frac{dh_0}{d\xi} \right) + \frac{3Bo(h_0 - 1)c_w}{h_0^3} + \frac{Bo}{h_0^3} - \frac{3MaBiBo}{2h_0(1 + Bi h_0)^2} \frac{dh_0}{d\xi}. \quad (40)$$

The third-order nonlinear evolution equation, Eq. (39) for $V \neq 0$ and Eq. (40) for $V = 0$, is solved in MATLAB R2022a with the shooting method and using the ode15s solver with the following initial conditions at $\xi \rightarrow 0$:

$$h_0 \rightarrow 1, \quad \frac{dh_0}{d\xi} \rightarrow 0, \quad \frac{d^2 h_0}{d\xi^2} \rightarrow 0. \quad (41)$$

The dynamics of the thin film of a thermoviscous fluid is governed by convective heat transfer (Bi), thermocapillary stresses (Ma), Bond number, and thermoviscous effects. Shown in Fig. 2 are the traveling wave profiles obtained by solving Eq. (40) for different values of the Marangoni numbers, and as expected, a larger value of Ma leads to a thicker capillary ridge. Plotted in Fig. 3 is the variation in fluid viscosity radially across the film thickness. The dimensionless viscosity at the surface of a solid cylinder is unity due to how it has been scaled. However, for positive thermoviscosity numbers, the dimensionless viscosity increases and decreases for negative thermoviscosity numbers as we move from the solid surface to the liquid-air interface. Notably, a viscosity gradient exists across the film thickness for a nonzero value of V . The steepness of the gradient is controlled by the Biot number, and it strongly affects the traveling wave profile.

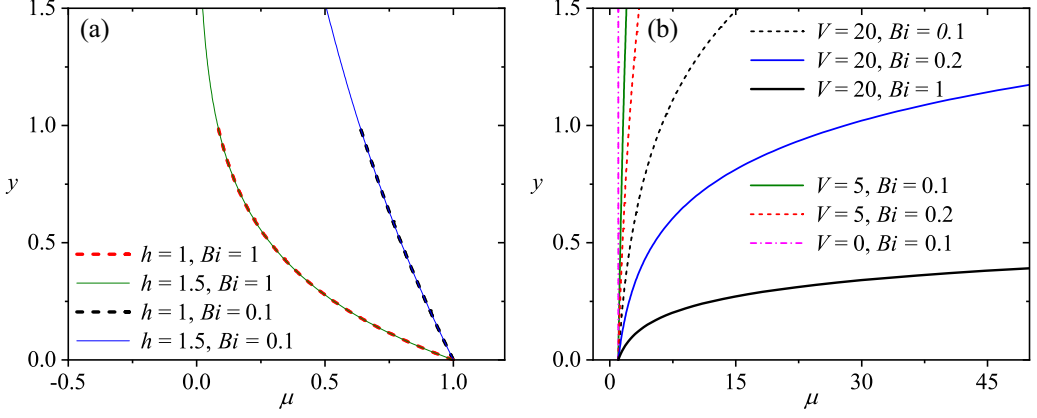


FIG. 3. Variation in dimensionless viscosity (μ) with the radial direction (y). (a) For different film heights and Biot numbers with $V = -5$ (cooler substrate), and (b) for different thermoviscosity numbers ($V > 0$) and Biot numbers.

B. Thermal effects on the traveling wave solution

The effect of the Marangoni number on the maximum amplitude of the wave profile (h_{\max}) and the wave speed (c_w) is shown in Fig. 4(a). The thermocapillary stress drives the fluid from high-temperature areas to low-temperature areas. Therefore, increased thermocapillary stress due to larger values of the Marangoni number leads to a thicker ridge. Increased wave amplitude enhances the gravitational force acting on the ridge, thereby increasing wave speed monotonically as a function of Ma . The effect of Bond number (Bo) is shown in Fig. 4(b). In the case of smaller Bond numbers, the beads grow to a large size due to strong capillary pressure and travel faster down the cylinder with a high velocity due to gravity. The figure shows that the steady-state solution does not exist for $Bo < 0.6$, while for larger values, the wave speed decreases as the capillary pressure decreases. This critical value of Bo is consistent with the earlier studies by Kalliadasis and Chang [12] and Yu and Hinch [2] which suggested that a steady-state solution is not possible for Bond number $Bo < 0.59$. In the work of Kalliadasis and Chang [12], a mathematical model based on the lubrication approximation was developed, and it was observed that small disturbances became very large size droplets within finite time for $Bo < 0.59$. On the other hand, for values of Bond

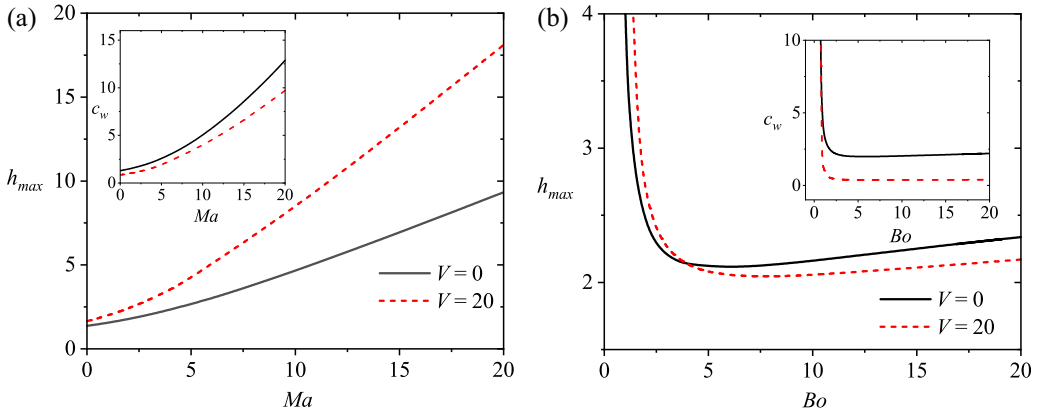


FIG. 4. Traveling wave amplitude (h_{\max}) and wave speed (c_w), (a) vs Ma for $Bi = 0.1$ and $Bo = 2$, and (b) vs Bo for $Ma = 2$ and $Bi = 1.0$.

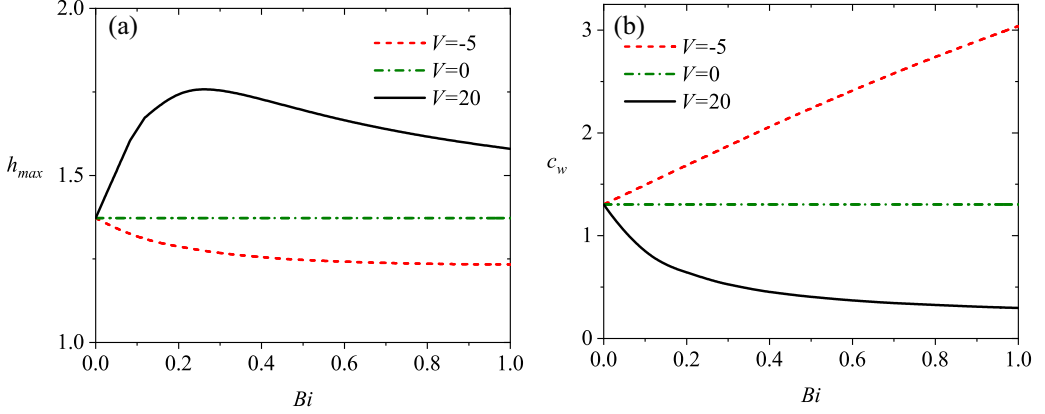


FIG. 5. Effect of Biot number for $V = -5$ and $V = 20$ on (a) wave amplitude (h_{\max}) and (b) speed (c_w). Other parameters are $Ma = 0$ and $Bo = 2$.

number greater than this value, the initial disturbances transformed into solitary waves. The critical value of Bo seems weakly dependent on the thermoviscous effect. For much larger values of Bo , the amplitude and wave speed again start to increase due to an increase in the effect of gravity. While the overall qualitative effects are similar, a quantitative variation is observed for different values of the thermoviscous number.

Thermoviscous effects with a varying Biot number on the maximum film thickness (h_{\max}) and wave speed (c_w) are shown in Figs. 5(a) and 5(b). This dimensionless parameter plays a vital role in governing the thermal behavior of the film by regulating the heat flux through the film. For $Bi \rightarrow 0$, convection heat flux from the film into the air becomes negligible, resulting in a uniform temperature (equal to the solid surface temperature) throughout the fluid. In the absence of temperature gradients across the thickness of the film, thermoviscous effects do not affect the dynamics. This situation can be observed in Figs. 5(a) and 5(b) at zero Biot number, where all the lines corresponding to different values of V coincide. Further, a nonzero value of the Biot number introduces temperature gradients in the system. However, these temperature gradients will not affect the flow characteristics for weakly thermoviscous fluid without Marangoni stresses. Hence, no variation is observed with the value of Biot number for $V = 0$ in Figs. 5(a) and 5(b). It is observed that for $V > 0$ the ridge height increases up to some value of the Biot number and then starts to decrease. This is due to an increased viscosity gradient at the liquid-gas interface with increase in the Biot number (enhanced convective cooling) up to a moderate value, leading to a larger capillary ridge. With a further increase in the Biot number, the ridge height decreases due to an overall increase in the average viscosity across the film, as can be seen in Fig. 3. This overall increase in the viscosity is the reason for a monotonic decrease in the wave speed, as indicated in Fig. 5(b) for $V > 0$. The trend of maximum film thickness and wave speed with increasing value of V is shown in Fig. 6. For a cooled cylinder with $V \ll 0$, the liquid-air interface is at the ambient temperature T_{∞} , causing a sharp decrease in viscosity near the interface. As V becomes more negative, the height decreases while the wave speed increases. A semilog graph is used in Fig. 6(b) because the variations in wave speed are very large for $V < 0$ and small for $V > 0$.

IV. LINEAR STABILITY ANALYSIS

Linear stability analysis of the steady-state film profile $h_0(\xi)$ is performed for a fast-moving solitary drop by introducing a small perturbation in the film evolution equation and by putting $h(\xi, \theta, t) = h_0(\xi) + \delta h_1(\xi, \theta, t)$, where $h_1(\xi, \theta, t) = \hat{h}_1(\xi) \exp(\beta t + iq\theta)$. The viscosity and interfacial temperature will also vary as the perturbation is introduced in the film thickness. In the

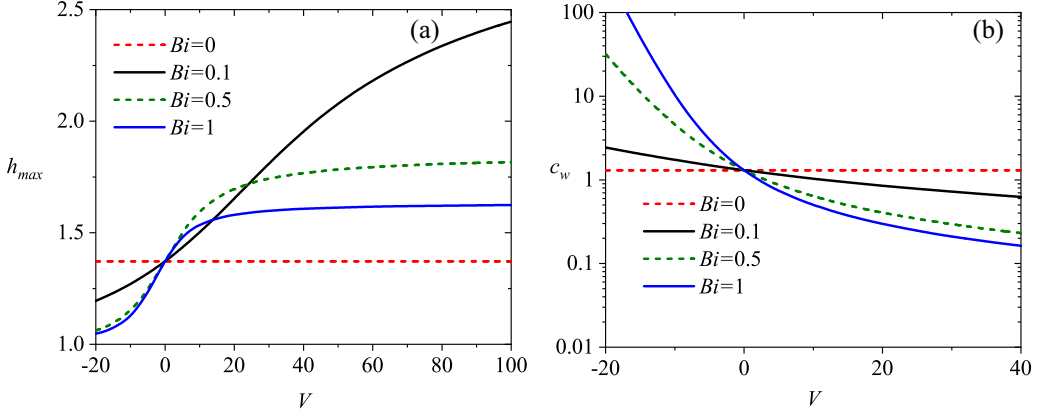


FIG. 6. Effect of thermoviscous parameter on (c) traveling wave amplitude and (d) wave speed for varying Bi . Other parameters are $Ma = 0$ and $Bo = 2$.

disturbance term, q represents the azimuthal wave number and β is the growth rate of perturbation:

$$\begin{aligned} T^i(\xi, \theta, t) &= T_0^i(\xi) + \delta T_1^i(\xi) h_1(\xi, \theta, t), \\ \eta(\xi, \theta, t) &= \eta_0(\xi) + \delta \eta_1(\xi) h_1(\xi, \theta, t), \end{aligned}$$

where

$$\begin{aligned} T_0^i &= \frac{1}{1 + Bi h_0}, \quad T_1^i = -\frac{Bi}{(1 + Bi h_0)^2}, \\ \eta_0 &= \frac{V Bi}{1 + Bi h_0}, \quad \eta_1 = -\frac{V Bi^2}{(1 + Bi h_0)^2}. \end{aligned} \quad (42)$$

The linear stability equation is obtained by collecting $O(\delta)$ terms after linearization of Eq. (37), and the definition h_1 is used to obtain

$$\mathbb{L}_0 \hat{h}_1 + \mathbb{L}_1 \hat{h}_{1\xi} + \mathbb{L}_2 \hat{h}_{1\xi\xi} + \mathbb{L}_3 \hat{h}_{1\xi\xi\xi} + \mathbb{L}_4 \hat{h}_{1\xi\xi\xi\xi} = \beta \hat{h}_1. \quad (43)$$

Here, the subscript ξ denotes partial derivative with regard to ξ , and \mathbb{L}_i is a linear operator for the i th-order derivative of \hat{h}_1 . The stability equation can be solved by using the boundary conditions $\hat{h}_{1\xi} = 0$ and $\hat{h}_{1\xi\xi\xi} = 0$ at $\xi = 0$, and $\xi = \infty$ [21,24–26]:

$$\begin{aligned} \mathbb{L}_0 &= -D_\xi - Ma [BT_{0\xi\xi}^i + AT_{1\xi\xi}^i + A_\xi T_{1\xi}^i + T_{0\xi}^i B_\xi] - Bo^{-1} [D(h_{0\xi\xi} + h_{0\xi\xi\xi\xi}) + D_\xi(h_{0\xi} + h_{0\xi\xi\xi})] \\ &\quad + q^2 \left(\frac{C}{Bo} + Ma AT_1^i - \frac{q^2 C}{Bo} \right), \end{aligned}$$

$$\mathbb{L}_1 = c_w - (D + Ma A_\xi T_1^i + Ma T_{0\xi}^i B) - Bo^{-1} [D(h_{0\xi} + h_{0\xi\xi\xi}) + C_\xi] + \frac{q^2 C_\xi}{Bo} - 2AMa T_{1\xi}^i,$$

$$\mathbb{L}_2 = -Ma AT_1^i - \frac{C}{Bo} + \frac{2Cq^2}{Bo},$$

$$\mathbb{L}_3 = -\frac{C_\xi}{Bo}, \quad \mathbb{L}_4 = -\frac{C}{Bo},$$

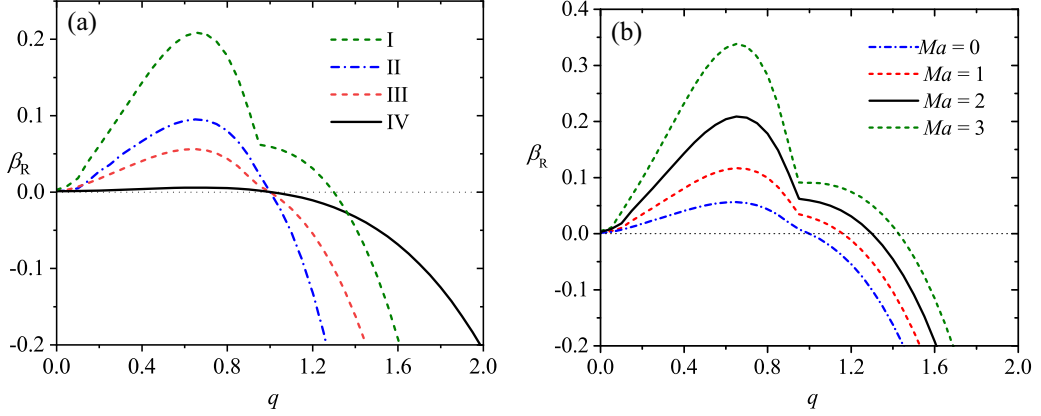


FIG. 7. Leading growth rate β_R is plotted vs wave number, q . (a) The parameter values $[Ma, V, Bo]$ are I = $[2, 20, 2]$, II = $[0, -5, 2]$, III = $[0, 20, 2]$, and IV = $[0, 20, 10]$, while $Bi = 0.2$; (b) the effect of Marangoni number. The parameter values are $Bo = 2, V = 20, Bi = 0.2$.

where

$$\begin{aligned}
 A &= -\left[\frac{h_0}{\eta_0} - \frac{1}{\eta_0^2} + \frac{\exp(-\eta_0 h_0)}{\eta_0^2} \right], \\
 B &= -\left[-\frac{\eta_1 h_0}{\eta_0^2} + \frac{1}{\eta_0} + \frac{2\eta_1}{\eta_0^3} - \exp(-\eta_0 h_0) \left(\frac{1}{\eta_0} + \frac{\eta_1 h_0}{\eta_0^2} + \frac{2\eta_1}{\eta_0^3} \right) \right], \\
 C &= \left[\frac{h_0^2}{\eta_0} + \frac{2A}{\eta_0} \right], \\
 D &= \left[-\frac{h_0^2 \eta_1}{\eta_0^2} + \frac{2h_0}{\eta_0} + \frac{2B}{\eta_0} - \frac{2A\eta_1}{\eta_0^2} \right].
 \end{aligned}$$

For a system with weak thermoviscous effects ($V \rightarrow 0$), coefficients used in Eq. (43) reduce to much simpler forms as

$$\begin{aligned}
 A &= -\frac{h_0^2}{2}, \quad B = -h_0, \\
 C &= \frac{h_0^3}{3}, \quad D = h_0^2.
 \end{aligned}$$

The stability equation (43) for $V = 0$ is identical to the one obtained by Ding and Wong [15]. Discretization of Eq. (43) along with the boundary conditions using a fourth-order central difference scheme results in an eigenvalue problem of the form $\mathbb{L}\hat{\mathbf{h}}_1 = \beta\hat{\mathbf{h}}_1$, which is solved numerically. Here \mathbb{L} represents an autonomous linear operator which depends on the base solution. Eigenvalues are obtained for each wave number q in MATLAB R2022a using the eig function. The leading eigenvalue of the linear operator $\beta = \beta_R + i\beta_I$ is reported here as a function of the wave number q , where β_R is the real part and hence quantifies the growth rate of the disturbance and β_I is the imaginary part. The system is linearly unstable if $\beta_R > 0$ for any wave number.

Dispersion curves are plotted in Fig. 7. The parameter values are chosen as $Bo = 2, V = 20, Bi = 0.2$, and $Ma = 0$ and then varied individually, keeping other parameters fixed, to quantify the effect of the varied parameter on the dispersion curves. As indicated in Fig. 7(a), increasing the value of the Bond number to $Bo = 10$ decreases the growth rate of the disturbance, caused by a reduction in the capillary pressure due to reduced surface tension compared to gravity. A cooled substrate

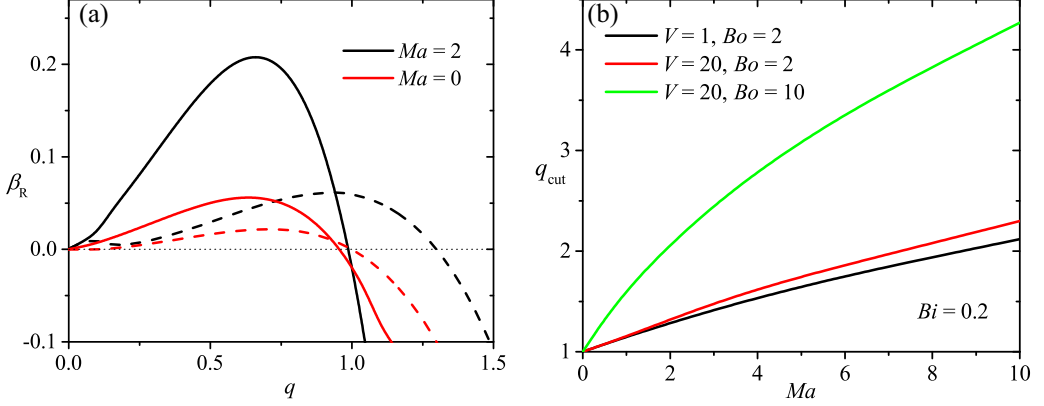


FIG. 8. (a) Dispersion curves corresponding to two leading modes in the absence ($Ma = 0$) and presence ($Ma = 2$) of thermocapillary stress. Here the solid lines correspond to the first mode and the dashed lines represent the second mode. (b) Cut-off wave number q_{cut} as a function of Ma . The other parameter values are fixed as $Bo = 2$, $V = 20$, $Bi = 0.2$ unless stated otherwise in the legends.

is shown to destabilize the film further, as quantified by changing the thermoviscous parameter to $V = -5$. The thermocapillary effect with $Ma = 2$ leads to a significant increase in the growth-rate values. For a nonzero Marangoni number, the thermocapillary stress acts on the perturbed surface, inducing the fluid flow into the crests, leading to further perturbation growth. As a result, we observe a monotonic increase in the maximum growth rate with increasing Marangoni number, as illustrated in Fig. 7(b). These effects are qualitatively similar to those reported in Khanum and Tiwari [21] for Rayleigh-plateau-type instability.

An interesting observation from Fig. 7 is that the wave number beyond which the film is unstable, termed the cut-off wave number, remains about $q_{cut} \simeq 1$ when the thermocapillary effect is absent, i.e., $Ma = 0$. With a nonzero value of Ma , the dispersion curve shows a sudden change in slope, indicating a change in the instability mode, and $q_{cut} > 1$ is obtained. Shown in Fig. 8(a) are the growth rates of two leading modes (first two largest eigenvalues of the linear operator) as a function of wave number q for $Ma = 0$ (no thermocapillary stress) and $Ma = 2$. Even in the absence of the thermocapillary stress, both modes exist; however, the first mode always dominates the second mode except for $q \geq 1$, where the second mode dominates but the growth rate has gone negative for those wave numbers. On the other hand, for $Ma = 2$, the second mode starts dominating for $q \geq 1$ and remains unstable, while the first mode becomes stable for these wave numbers. Shown in Fig. 8(b) are the cut-off wave-number values as a function of Ma for various values of V and Bo keeping $Bi = 0.2$ fixed. Clearly, q_{cut} is a monotonically increasing function of Ma . Also, increasing the values of V and Bo further enhances the cut-off wave number.

To understand these two modes appearing in the dispersion curves, the eigenvectors are plotted in Fig. 9, corresponding to the leading eigenvalues at $q = 0.65$ and $q = 1.1$, shown in Fig. 7(a). Shown in Fig. 9(a) are the eigenvectors for $Ma = 0$, while in Fig. 9(b), eigenvectors are shown for $Ma = 2$. The corresponding base film-thickness profile is also superimposed. It is clear that for the first mode, which is dominant at $q = 0.65$, the disturbance is located very close to the capillary ridge, while it decays to zero far away from the ridge. This implies that once the disturbance creates asymmetry in the azimuthal direction at the ridge, the thicker region will flow down due to gravity, causing the growth of the instability. Thus this first mode will be termed as the gravity mode. For the second mode, which is dominant for $q > 1$, while the disturbance is located at the ridge, it does not decay downstream and attains a constant value. While this dominant second mode is stable for $Ma = 0$, it is unstable for $Ma = 2$. This implies that such a disturbance present far away from the ridge can grow only in the presence of the thermocapillary effect. This mode will be termed the

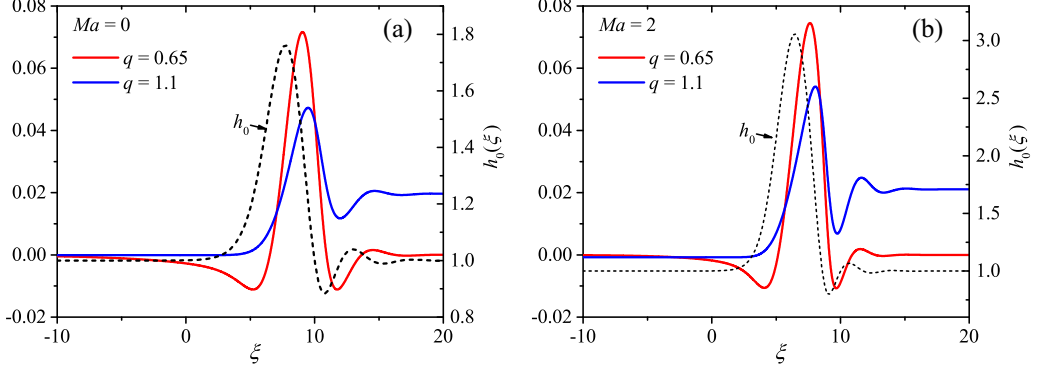


FIG. 9. Eigenvectors corresponding to the leading eigenvalues in Fig. 7(a) for $q = 0.65$ and $q = 1.1$ for (a) $Ma = 0$ and (b) $Ma = 2$. The corresponding base film-thickness profile $h_0(\xi)$ is superimposed as a dotted curve and is plotted on the secondary y axis.

thermocapillary mode. Therefore, the cut-off wave numbers and the shape of the eigenvectors for different modes will have important implications for the disturbance pattern that finally grows on the film, as illustrated in the next section with the help of nonlinear computations.

V. NONLINEAR SIMULATIONS

This section presents results for the nonlinear numerical calculation performed by solving the complete time-dependent evolution equation, Eq. (37). The finite element method-based software COMSOL 6.0 is utilized to perform the computations. The computational domain in the azimuthal direction extends from $\theta = 0$ to $\theta = 2\pi$ and uses periodic boundary conditions at the two ends. A two-dimensional computational domain of 60 units of axial length with about 10^4 mesh points is utilized. The absolute tolerance of 10^{-9} is imposed during the time-dependent computations. A sinusoidal perturbation with a small amplitude of 10^{-3} and a prescribed wave number is introduced into the base state $h_0(\xi)$ as the initial condition. In the upstream axial direction, a Dirichlet boundary condition $h(\theta, \xi = 0, t) = 1$, $h_\xi(\theta, \xi = 0, t) = 0$ is imposed, while the soft condition [21] $h_\xi(\theta, \xi \rightarrow \infty, t) = 0$, $h_{\xi\xi\xi}(\theta, \xi \rightarrow \infty, t) = 0$ is imposed at the downstream boundary. The nonlinear growth of the perturbation is quantified by the amplification ratio φ , where

$$\varphi = \ln \left[\frac{\|h(\theta, \xi, t) - h_0(\xi)\|}{\|h(\theta, \xi, t=0) - h_0(\xi)\|} \right], \quad (44)$$

and $\|\cdot\|$ represents the L_2 norm.

The disturbance growth obtained from the nonlinear model is plotted in Fig. 10 for $Ma = 2$, $Bi = 0.2$, $Bo = 2$, and $V = 20$. The eigenvalue curve obtained from linear stability for this set of parameter values is shown in Fig. 8(a). It was seen earlier that the maximum eigenvalue was obtained at $q = 0.65$, and the gravity mode dominated at this wave number. The thermocapillary mode became unstable for $q \geq 1$. The nonlinear growth curve for $q = 0.65$ shows that initially, the disturbance grows with a slope decreasing with time; however, after a certain time, the growth rate, given by $\beta_{NL} = d\varphi/dt$, increases and becomes constant. The constant value was surprisingly not equal to the eigenvalue at $q = 0.65$ (the maximum eigenvalue of the dispersion curve) but to that found at $q = 1$. The curve for $q = 1$ expectedly quickly attained the growth rate $\beta_{NL} = 0.06$, equal to the eigenvalue at $q = 1$. Similarly, the growth curve for $q = 1.1$ followed a similar trend and attained the growth rate prescribed by the eigenvalue at $q = 1$. All three curves attained saturation after the exponential growth phase of the disturbance; however, the saturation was attained later for $q = 0.65$ as compared to the other two wave numbers shown in the plot.

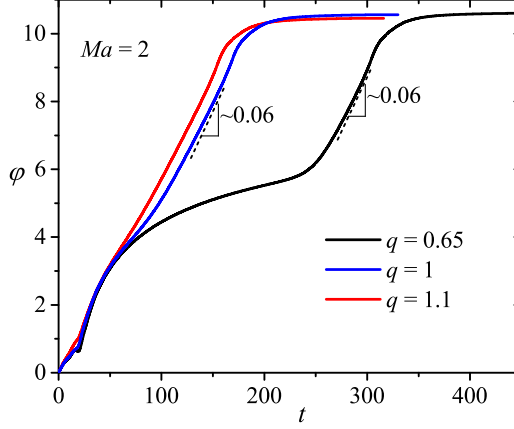


FIG. 10. Nonlinear growth of disturbance $\varphi(t)$ for $q = 0.65$, $q = 1$, and $q = 1.1$. The parameter values are fixed as $Ma = 2$, $Bi = 0.2$, $Bo = 2$, and $V = 20$.

To understand the growth patterns of the disturbance on the substrate with time, the nonlinear growth curves are shown in Fig. 11 along with the contours of film thickness $h(\xi, \theta, t)$. In the initial period there is no visible growth of the disturbance, and the film profile with a capillary ridge and no azimuthal dependence is seen in the figure, although the amplification ratio starts to increase, indicating the growth of disturbance from its initial value. For $250 \lesssim t \lesssim 320$, where the exponential growth rate (or linear growth rate in φ versus t plot) is observed, an asymmetric drop starts to appear, which grows in time. Such a drop is shown at $t = 300$ in the plot. During this exponential growth phase, the thermocapillary mode also comes into play, and rivulets also start to appear below the drop. These rivulets extend far downstream of the substrate. As time progresses, Marangoni stress pulls more fluid into the drop, making the drop and the rivulet thicker while the trough becomes thinner, as indicated at $t = 350$ in the plot. At the nonlinear saturation, $t = 400$, multiple drops appear while sliding down the substrate but remain confined to the rivulet. It is interesting to note that the axially asymmetric pattern thus obtained has a periodicity equal to the perimeter of the substrate. Thus, the growth rate in the exponential phase is equal to the eigenvalue at $q = 1$. Further, the growth of the disturbance seems to have been assisted by the thermocapillary

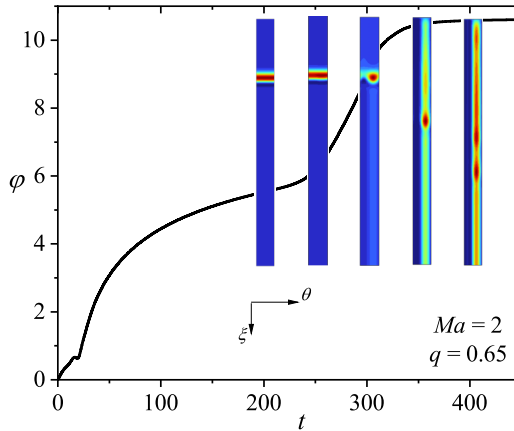


FIG. 11. Nonlinear growth of disturbance, $\varphi(t)$, corresponding to the parameters in Fig. 10 and $q = 0.65$. Also shown are the contours at $t = 200$, $t = 250$, $t = 300$, $t = 350$, and $t = 400$, illustrating the evolution of the disturbance with time.

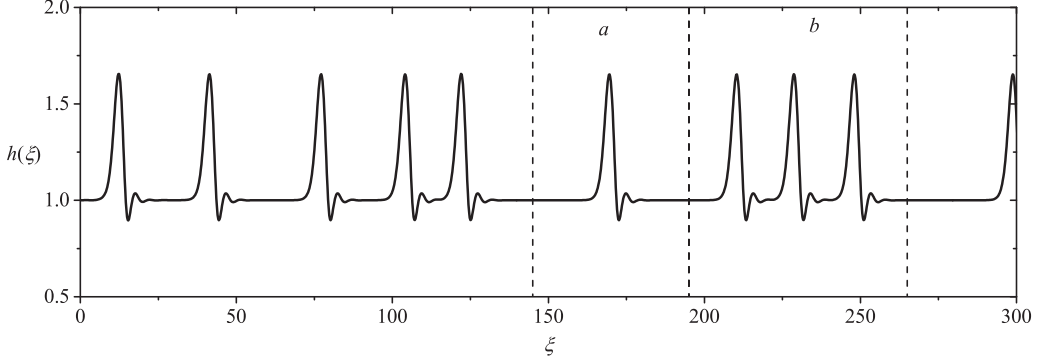


FIG. 12. Traveling waves obtained by performing nonlinear simulations of the time-dependent evolution equation following the methods of an earlier study [22]. The dimensionless parameters used for the study are $Bi = 0.1$, $Ma = 0$, $Bo = 2$, and $V = 20$.

mode, which leads to the formation of an asymmetric rivulet. For $Ma = 0$, the eigenvalue at $q = 1$ is close to zero. Therefore no asymmetric disturbance was observed in the nonlinear computations until $t = 1000$, although the dispersion curve predicts a maximum asymmetric disturbance growth of 0.21 at $q = 0.65$.

VI. DISCUSSION

A. Traveling wave solution

In the work of Kishal and Tiwari [22], a spatiotemporal study was carried out for the flow over a nonisothermal cylinder. It was shown that when a Gaussian disturbance is applied to a uniform film over a cylinder in a nonlinear stability analysis, the disturbance is saturated into a traveling wave after a sufficiently long time. In this section the traveling wave solution obtained using the shooting method is compared with the saturated disturbance obtained by the method of Kishal and Tiwari [22]. Using the same method outlined in their work, the wave obtained is shown in Fig. 12. Absolute tolerance of 10^{-7} is used. It can be observed that while the spacing between the neighboring peaks is not uniform, their structure is identical, as illustrated in regions *a* and *b* in the given figure. The traveling wave obtained through nonlinear time-dependent simulations is compared with the film profile obtained using the shooting method and is shown in Fig. 13. Notably, the film profiles showed an excellent agreement. The multiple peaks profile was also used to study its linear stability in the azimuthal direction. Although not shown here, the dispersion curves obtained for this profile also matched those for the single-peak traveling wave solution.

B. Streamlines

Streamlines are demonstrated in this section to visualize the flow. The stream function $\psi(y, \xi)$ is obtained by integrating the velocity field derived in Eq. (34) and utilizing the base solution obtained for the film profile. The value of the stream function ψ has been assigned the value zero at the solid wall, i.e., at $y = 0$:

$$\begin{aligned} \psi(y, \xi) = & \left(1 + Bo^{-1} \frac{dh_0}{d\xi} + Bo^{-1} \frac{d^3 h_0}{d\xi^3} \right) \\ & \times \left[\frac{(y - h_0)}{\eta^2} \exp(-\eta y) + 2 \frac{\exp(-\eta y)}{\eta^3} + \frac{(h_0 + y)}{\eta^2} - \frac{2}{\eta^3} - \frac{h_0 y}{\eta} \right] \\ & - Ma \frac{dT^i}{d\xi} \left(-\frac{y}{\eta} + \frac{1}{\eta^2} - \frac{\exp(-\eta y)}{\eta^2} \right) + c_w y. \end{aligned} \quad (45)$$

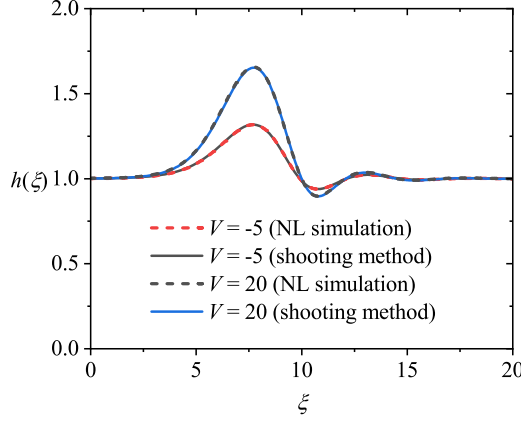


FIG. 13. Comparison of the film profile obtained through time-dependent simulations (indicated as NL simulation in the plot) and that obtained using a shooting method for $Bi = 0.1$, $Ma = 0$, and $Bo = 2$. Wave speeds obtained from both the methods are identical, i.e., $c_w = 1.49$ for $V = -5$ and $c_w = 0.85$ for $V = 20$.

Shown in Fig. 14 are the streamlines obtained for parameter values as used in Fig. 8(a). It was shown in Fig. 8(a) that for $Ma = 0$, only the gravity mode was unstable, for which the cut-off wave number was less than 1, and the disturbance was concentrated near the capillary ridge and decayed to zero away from it. On the other hand, the thermocapillary mode was stable. For $Ma = 2$, the thermocapillary mode was unstable and existed for $q > 1$, leading to interesting pattern formation. The pattern formed was similar to those shown in the case of the flow of a thin film over a nonuniformly heated flat substrate [24]. In that flow configuration, it has been shown that an unstable capillary ridge, caused by heterogeneous heating, is usually accompanied by closed streamlines, i.e., recirculations existed [27]. The similarity of the thermocapillary mode here with that in the case of the flat plate is also marked out due to the presence of closed streamlines for $Ma = 2$ as well as the absence of it for $Ma = 0$, as shown in Fig. 14. The presence of the closed streamlines near the capillary ridge in the base profile is, therefore, an indication of the presence of the thermocapillary mode.

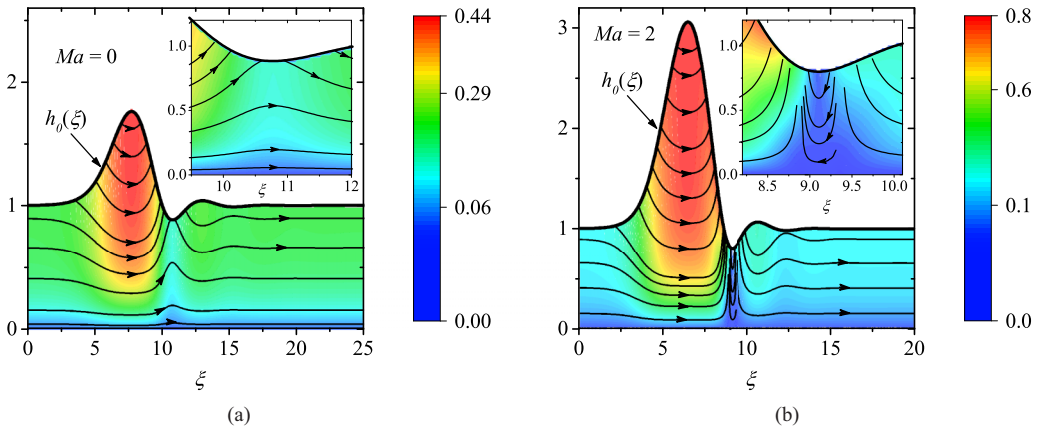


FIG. 14. Streamline plots for (a) $Ma = 0$, and (b) $Ma = 2$. The other parameters are $Bo = 2$, $Bi = 0.2$, and $V = 20$. The solid line is the corresponding base film profile with arrows representing the velocity direction. Velocity magnitude is shown using colored contours. The inset shows the zoomed view of the velocity profiles near the thinner region. Recirculation is seen in (b).

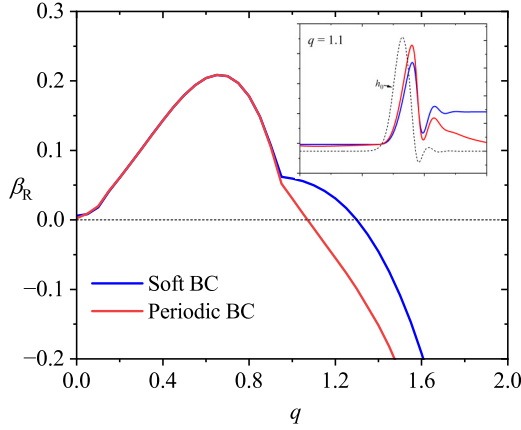


FIG. 15. Comparison of growth rate (β_R) vs wave number (q) for soft and periodic boundary conditions. Inset shows the eigenvectors for $q = 1.1$ corresponding to the two boundary conditions.

C. Soft versus periodic condition

In the linear and nonlinear stability results, the soft boundary conditions have been used in this study at the downstream boundary of the domain, consistent with the earlier works [21,24–26]. In this section the comparison of these results is shown with those obtained from the usual periodic boundary condition [17] along the streamwise direction. Shown in Fig. 15 is the comparison of the dispersion curves for the two boundary conditions. It is clear that the two curves overlap for $q \leq 1$, and the periodic condition yields stable modes for $q > 1$ while the unstable modes are obtained for the soft condition. The inset shows the eigenfunctions for the two boundary conditions at $q = 1.1$. It is evident that while the disturbance is sustained far downstream for the soft condition, the periodic condition forces the disturbance to decrease to match the upstream condition. It was shown in Fig. 9 that while for $q < 1$, the eigenfunction corresponding to the leading mode decayed to zero at both boundaries, for $q > 1$, the disturbance attained a constant nonzero value far downstream with the soft condition. Since the periodic boundary condition cannot capture the disturbance due to the thermocapillary mode, the dispersion curves differ for larger values of the wave numbers.

The comparison in the nonlinear growth computed using the two boundary conditions is shown in Fig. 16 for $q = 1.1$. While the linear stability yields the growth rate of $\beta_R = -0.0122$ and $\beta_R = 0.05$ for the periodic and soft boundary conditions, respectively, the nonlinear growth rate obtained here corresponds to the linear growth rate for $q = 1$. Thus, while the disturbance grows with $\beta_{NL} = 0.06$ for the soft condition, it is $\beta_{NL} = 0.036$ for the periodic condition. The film contours are also shown for the periodic condition at times $t = 200$ and $t = 250$. At $t = 200$, the asymmetric droplet has started to appear, and at the same time, undulations are present in the streamwise direction downstream from this droplet. While this droplet becomes more prominent at $t = 250$, other droplet-type structures start appearing downstream and the two structures are not aligned. It is also clear that due to the imposed periodicity, the downstream structure is feeding into the upstream droplet. The corresponding structures for the soft condition look similar to those shown in Fig. 11, wherein a single droplet appears and an asymmetric pattern evolves in the entire domain.

D. More nonlinear patterns

In this section the nonlinear computations are presented for a case where more than one droplet in the azimuthal direction is expected to form, i.e., the cut-off wave number $q_{\text{cut}} > 2$. Such a case is obtained with the parameter values $\text{Ma} = 3$, $\text{Bi} = 0.2$, $V = 20$, and $\text{Bo} = 10$. The cut-off wave number $q_{\text{cut}} \simeq 2.5$ for these values. The growth rates are found to be $\beta_R \simeq 0.177$ at $q = 1$,

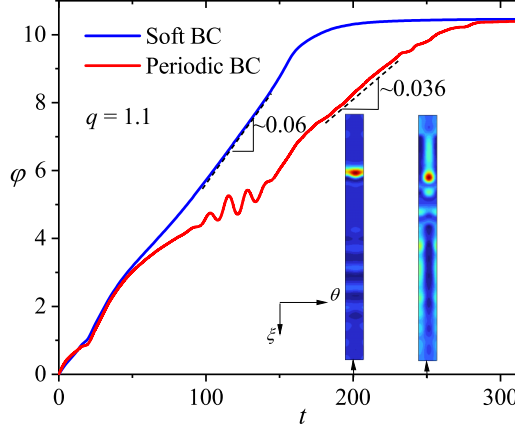


FIG. 16. Comparison of the nonlinear growth (φ) of disturbance ($q = 1.1$) for soft and periodic boundary conditions. Contours are shown for periodic conditions at $t = 200$ and $t = 250$.

$\beta_R \simeq 0.148$ at $q = 2$, and $\beta_R \simeq -0.43$ at $q = 3$. Clearly, the dominant growth is found at $q = 1$, while the disturbance with $q = 3$ is linearly stable. Interestingly, for $q = 1$ the leading eigenvector corresponded to the gravity mode (as discussed in Sec. IV), i.e., it decayed to zero far away from the capillary ridge, while the eigenvectors for $q = 2$ and $q = 3$ corresponded to the thermocapillary mode with a constant value downstream of the capillary ridge.

The nonlinear growth versus time is shown in Fig. 17 for the three different wave numbers. The growth curves in this plot, except that for $q = 3$, end at the time of rupture of the respective profiles. The wave numbers $q = 1$ and $q = 2$ recover their respective linear growth rates in the exponential growth region. The corresponding contour in Fig. 18 shows that for $q = 1$, a single localized drop forms as expected from the eigenvector and then slides downstream. For $q = 2$, the disturbance affects the flow downstream, forming two rivulets emanating from the capillary ridge. The pattern is consistent with the eigenvector shape and corresponds to the thermocapillary mode. The nonlinear growth curve for $q = 3$ shows a negative growth (or decaying growth) in the early times ($t < 7$), which is consistent with the linear stability prediction. Subsequently, it starts to

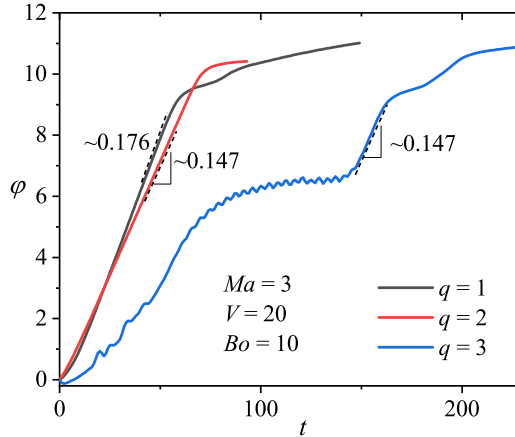


FIG. 17. Comparison of the nonlinear growth (φ) of disturbances with wave number $q = 1$, $q = 2$, and $q = 3$. The parameter values used for this result are $Ma = 3$, $Bi = 0.2$, $V = 20$, and $Bo = 10$. The growth rates obtained for these wave numbers are $\beta_R \simeq 0.177$ ($q = 1$), $\beta_R \simeq 0.148$ ($q = 2$), and $\beta_R \simeq -0.43$ ($q = 3$).

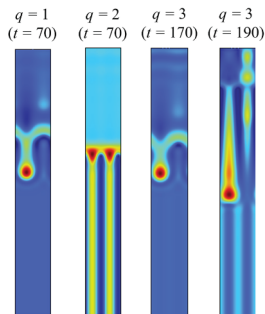


FIG. 18. Comparison of the nonlinear patterns corresponding to the growth (φ) shown in Fig. 17.

show positive growth. At $t \sim 100$ the growth reaches a brief saturation period with oscillations. An exponential growth appears between $t \sim 150$ and $t \sim 170$, whose rate is surprisingly equal to the leading eigenvalue at $q = 2$. The patterns for $q = 3$ are shown at two time instants in Fig. 18. Up to $t \sim 150$, a single droplet starts to form, similar to that observed for the case of $q = 1$. Subsequently, the droplet increases in width while moving downstream, forming two rivulets similar to the pattern obtained for the case of $q = 2$. In addition, interesting features appear upstream at the time that coincides with the oscillating saturation in the nonlinear growth curve. Thus the pattern obtained for $q = 3$ deviates significantly from what the linear stability analysis predicted. The geometrically imposed confinement forces the film to choose a suitable wavelength that grows over time and gets affected by other unstable modes.

VII. CONCLUSION

This study analyzed the stability of a traveling wave on the outside surface of a heated solid vertical cylinder. The coating thickness was considered much thinner than the radius of the cylinder, leading to employing the thin-film assumption to simplify the flow and energy equations. The effect of the thermal condition of the cylinder on the viscosity and surface tension was considered. The film viscosity was considered to vary exponentially with temperature. The traveling wave solutions in the axial direction were found in a moving reference frame using the shooting method. An increase in the thermocapillary effect led to an increase in the capillary ridge height and the wave speed of the traveling wave. The height of the capillary ridge increased with an increase in the thermoviscous effect while the wave speed decreased. The traveling wave solution could not be found for the value of the Bond number below a certain critical number. This critical number was found to depend weakly upon the thermoviscous parameter.

The stability of the traveling wave solution was performed by imposing a small perturbation in the azimuthal direction. Linear stability analysis showed the presence of two modes of instability. It was shown that at smaller wave numbers, the gravity mode exists, while in the presence of the thermocapillary effect, a thermocapillary mode also exists but at larger wave numbers. The eigenvector indicated that gravity affects the capillary ridge, while the thermocapillary mode leads to perturbation growth far downstream from the capillary ridge. While other parameters like the Bond number and thermoviscous parameters increased the growth rate of the gravity mode, only the Marangoni number increased the growth rate of the thermocapillary mode. The cutoff or the critical wave number also increased with an increase in the Marangoni number and the thermoviscous parameter at a constant Marangoni number.

The nonlinear stability analysis showed that the mode chosen to generate the disturbance pattern does not correspond to the largest eigenvalue of the dispersion curve, but it is governed by the geometric confinement. Insignificant growth in the disturbance was observed for the cases where cut-off wave number was less than unity. For the cases where cut-off wave number was slightly more

than unity, the growth-rate and saturated disturbance pattern corresponded to wavelengths equal to the cylinder's circumference. For the imposed disturbance corresponding to the integer wave numbers as the initial condition, the positive growth rate obtained from the nonlinear simulations matched those predicted from the linear stability analysis. For the case when the cut-off wave number was greater than 2, an interesting nonlinear pattern was obtained when an initial disturbance corresponding to the wave number beyond cut-off value was imposed. These nonlinear patterns are caused by an interesting interplay between the gravity mode and thermocapillary mode that could not be captured by the usual periodic boundary condition in the nonlinear simulations and requires the soft conditions.

-
- [1] R. Craster and O. Matar, On viscous beads flowing down a vertical fibre, *J. Fluid Mech.* **553**, 85 (2006).
 - [2] L. Yu and J. Hinch, Drops of power-law fluids falling on a coated vertical fibre, *J. Fluid Mech.* **751**, 184 (2014).
 - [3] D. Quéré, Thin films flowing on vertical fibers, *Europhys. Lett.* **13**, 721 (1990).
 - [4] I. Kliakhandler, S. H. Davis, and S. Bankoff, Viscous beads on vertical fibre, *J. Fluid Mech.* **429**, 381 (2001).
 - [5] C. T. Gabbard and J. B. Bostwick, Asymmetric instability in thin-film flow down a fiber, *Phys. Rev. Fluids* **6**, 034005 (2021).
 - [6] H. Gau, S. Herminghaus, P. Lenz, and R. Lipowsky, Liquid morphologies on structured surfaces: From microchannels to microchips, *Science* **283**, 46 (1999).
 - [7] M. Binda, D. Natali, A. Iacchetti, and M. Sampietro, Integration of an organic photodetector onto a plastic optical fiber by means of spray coating technique, *Adv. Mater.* **25**, 4335 (2013).
 - [8] A. Kundan, T. T. T. Nguyen, J. L. Plawsky, P. C. Wayner, Jr., D. F. Chao, and R. J. Sicker, Condensation on highly superheated surfaces: Unstable thin films in a wickless heat pipe, *Phys. Rev. Lett.* **118**, 094501 (2017).
 - [9] S. Haefner, M. Benzaquen, O. Bäumchen, T. Salez, R. Peters, J. D. McGraw, K. Jacobs, E. Raphaël, and K. Dalnoki-Veress, Influence of slip on the plateau-Rayleigh instability on a fibre, *Nat. Commun.* **6**, 7409 (2015).
 - [10] H.-C. Chang and E. A. Demekhin, Mechanism for drop formation on a coated vertical fibre, *J. Fluid Mech.* **380**, 233 (1999).
 - [11] C. Duprat, C. Ruyer-Quil, S. Kalliadasis, and F. Giorgiutti-Dauphiné, Absolute and convective instabilities of a viscous film flowing down a vertical fiber, *Phys. Rev. Lett.* **98**, 244502 (2007).
 - [12] S. Kalliadasis and H.-C. Chang, Drop formation during coating of vertical fibres, *J. Fluid Mech.* **261**, 135 (1994).
 - [13] G. F. Dietze, G. Lavalley, and C. Ruyer-Quil, Falling liquid films in narrow tubes: Occlusion scenarios, *J. Fluid Mech.* **894**, A17 (2020).
 - [14] A. Frenkel, Nonlinear theory of strongly undulating thin films flowing down vertical cylinders, *Europhys. Lett.* **18**, 583 (1992).
 - [15] Z. Ding and T. N. Wong, Three-dimensional dynamics of thin liquid films on vertical cylinders with Marangoni effect, *Phys. Fluids* **29**, 011701 (2017).
 - [16] T. C. Kumawat and N. Tiwari, Stability analysis of the rimming flow inside a uniformly heated rotating horizontal cylinder, *Phys. Fluids* **29**, 032102 (2017).
 - [17] Z. Ding, R. Liu, T. N. Wong, and C. Yang, Absolute instability induced by Marangoni effect in thin liquid film flows on vertical cylindrical surfaces, *Chem. Eng. Sci.* **177**, 261 (2018).
 - [18] T. C. Kumawat and N. Tiwari, Flow and stability of a gravity-driven thin film over a locally heated porous wall, *Phys. Fluids* **32**, 092106 (2020).
 - [19] T. C. Kumawat and N. Tiwari, Hydrodynamic stability of thermoviscous liquid film inside a rotating horizontal cylinder: Heating and cooling effects, *Phys. Fluids* **30**, 032103 (2018).

- [20] G. A. Leslie, S. Wilson, and B. Duffy, Thermoviscous coating and rimming flow, [Q. J. Mech. Appl. Math.](#) **65**, 483 (2012).
- [21] S. Khanum and N. Tiwari, Gravity-driven thermoviscous liquid film down a heated or cooled vertical cylinder, [Phys. Rev. Fluids](#) **5**, 094005 (2020).
- [22] D. Kishal and N. Tiwari, Thick film flowing down a non-isothermal vertical cylinder, [J. Eng. Math.](#) **137**, 2 (2022).
- [23] S. Wilson and B. Duffy, Strong temperature-dependent-viscosity effects on a rivulet draining down a uniformly heated or cooled slowly varying substrate, [Phys. Fluids](#) **15**, 827 (2003).
- [24] N. Tiwari and J. M. Davis, Nonmodal and nonlinear dynamics of a volatile liquid film flowing over a locally heated surface, [Phys. Fluids](#) **21**, 102101 (2009).
- [25] C. Bielarz and S. Kalliadasis, Time-dependent free-surface thin film flows over topography, [Phys. Fluids](#) **15**, 2512 (2003).
- [26] H.-C. Chang, E. A. Demekhin, and S. S. Saprikin, Noise-driven wave transitions on a vertically falling film, [J. Fluid Mech.](#) **462**, 255 (2002).
- [27] N. Tiwari, Z. Mester, and J. M. Davis, Stability and transient dynamics of thin liquid films flowing over locally heated surfaces, [Phys. Rev. E](#) **76**, 056306 (2007).